Yu C, Li Z, Penna NT.

Interferometric synthetic aperture radar atmospheric correction using a GPS-based iterative tropospheric decomposition model.

***Remote Sensing of Environment* 2017**

DOI: https://doi.org/10.1016/j.rse.2017.10.038

Remote Sensing of Environment xxx (xxxx) xxx–xxx

Contents lists available at ScienceDirect

Remote Sensing of Environment

journal homepage: www.elsevier.com/locate/rse

Interferometric synthetic aperture radar atmospheric correction using a GPS-based iterative tropospheric decomposition model

Chen Yu, Zhenhong Li*, Nigel T. Penna

School of Engineering, Newcastle University, Newcastle upon Tyne NE1 7RU, UK

ARTICLE INFO

Keywords:
InSAR
GPS
Tropospheric delay
Atmospheric correction
Performance indicator
Station spacing

ABSTRACT

Atmospheric effects represent one of the major error sources of repeat-pass Interferometric Synthetic Aperture Radar (InSAR), and could mask actual displacements due to tectonic or volcanic deformation. The tropospheric delays vary both vertically and laterally and can be considered as the sum of (i) a vertically stratified component highly correlated with topography and (ii) a turbulent component resulting from turbulent processes in the troposphere varying both in space and time. In this paper, we outline a framework to routinely use pointwise GPS data to reduce tropospheric effects on satellite radar measurements. An Iterative Tropospheric Decomposition (ITD) model is used and further developed to separate tropospheric stratified and turbulent signals and then generate high-resolution correction maps for SAR interferograms. Cross validation is employed to assess the performance of the ITD model and act as an indicator to users of when and where correction is feasible. Tests were carried out to assess the impact of GPS station spacing on the ITD model InSAR correction performance, which provides insights into the trade-off between station spacing and the achievable accuracy. The application of this framework to Sentinel-1A interferograms over the Southern California (USA) and Southern England (UK) regions shows approximately 45–78% of noise reduction even with a sparse (~50–80 km station spacing) GPS network and/or with strong and non-random tropospheric turbulence. This is about a 50% greater improvement than previous methods. It is believed that this framework could lead to a generic InSAR atmospheric correction model while incorporating continuous and global tropospheric delay datasets, e.g. numerical weather models.

1. Introduction

Radar signals are delayed when passing through the troposphere, especially the wet delay part due to atmospheric water vapor, which is a major Interferometric Synthetic Aperture Radar (InSAR) error source when mapping the Earth's surface movements (e.g. Massonnet et al., 1994; Massonnet and Feigl, 1998; Williams et al., 1998; Simons and Rosen, 2007; Ding et al., 2008; Hooper et al., 2012; Jolivet et al., 2014). Variations in pressure, temperature, and relative humidity in the troposphere result in up to 15–20 cm errors on an interferogram and can often be much larger than the tectonic signals of interest (e.g. Hooper et al., 2012; Bekaert et al., 2015b). Jolivet et al. (2014) showed that by removing the stratified tropospheric delay, unwrapping is greatly improved over rough terrain and the trade-offs between the long-wavelength deformation signals and the different sources of noise improve. Hence mitigating InSAR atmospheric artifacts is crucial to study low-amplitude, long-wavelength deformation fields such as those due to inter-seismic strain accumulation or post-seismic motions (e.g. Elliott et al., 2008; Walters et al., 2013), volcanoes (e.g. Lu et al., 2010), urban subsidence (e.g. Crosetto et al., 2002; Chen et al., 2016) and permafrost (e.g. Chen et al., 2013; Short et al., 2014).

Based on the dynamic nature of the troposphere, numerous attempts have been made on the quantification and mitigation of InSAR tropospheric effects which are usually divided into two types. The first is to characterize the statistical properties of phase delays and separate stochastic noise from ground motion signals, including SAR interferogram stacking (e.g. Ferretti et al., 2011), correlation analysis between interferometric phases and topography (e.g. Fruneau and Sarti, 2000; Elliott et al., 2008; Shirzaei and Bürgmann, 2012), spatial-temporal filtering of the time series (e.g. Ferretti et al., 2001; Hooper et al., 2004; Ferretti et al., 2011), and power law analysis (e.g. Bekaert et al., 2015a). Their main advantage is that no external data are required. However, both stacking and spatial-temporal filtering ignore that tropospheric delays are not Gaussian distributed and they can degrade the temporal resolution of InSAR measurements and mask useful geophysical signals (Doin et al., 2009). Correlation analysis methods assume a linear or non-linear (e.g. exponential) relation between phase and elevation across the whole interferogram (Elliott et al., 2008; Shirzaei and

* Corresponding author.
E-mail address: Zhenhong.Li@newcastle.ac.uk (Z. Li).

http://dx.doi.org/10.1016/j.rse.2017.10.038
Received 15 March 2017; Received in revised form 22 August 2017; Accepted 21 October 2017

Bürgmann, 2012), or a piece-wise slope correction over multiple windows (e.g. Béjar-Pizarro et al., 2013), and are hence limited as they ignore the spatial variability of tropospheric signals. It is also hard to estimate a constant reference phase within windows as other phase contributions bias the estimate. Bekaert et al. (2015a) utilized a power law relation which accounts for a spatially-varying tropospheric signal in the presence of deformation. However, other contamination signals from the turbulent troposphere and orbit errors cannot be handled and manual interactions are required, such as a priori information about the spatial extent of deformation throughout time for the selection of the non-deforming band (Bekaert et al., 2015b).

The second type of tropospheric mitigation is the correction of atmospheric effects using external datasets including meteorological data (e.g. Delacourt et al., 1998; Jolivet et al., 2011), Moderate Resolution Imaging Spectroradiometer (MODIS) (e.g. Li et al., 2005; Li et al., 2009), MEdium Resolution Imaging Spectrometer (MERIS, e.g. Li et al., 2006a; Li et al., 2012), numerical weather models such as from the European Centre for Medium-Range Weather Forecasts (ECMWF, e.g. Walters et al., 2013) and Global Positioning System (GPS, e.g. Li et al., 2006a; Onn and Zebker, 2006; Reuveni et al., 2015; Houlié et al., 2016). MERIS and MODIS provide high spatial resolution water vapor maps with 1.0–1.2 mm RMS agreements with radiosondes and GPS, but they are restricted by the presence of clouds (Li et al., 2009). ECMWF is globally available but suffers from coarse temporal and spatial resolution and failures during periods of atmospheric turbulence (Jolivet et al., 2014). Of all the external information, GPS provides the highest temporal resolution (e.g. 5 min) of Zenith Total Delay (ZTD) measurements, and hence avoids additional uncertainties due to the time differences between water vapor and radar measurements when using MODIS, MERIS or ECMWF (Li et al., 2009; Walters et al., 2013). Such high temporal resolution measurements are particularly valuable in rainy seasons or for coastal areas where water vapor temporal fluctuations can be substantial (e.g. Rao et al., 1996; Bastin et al., 2007; Huang and Wen, 2014). Standard deviations between pointwise GPS water vapor measurements and those from radiosondes and microwave radiometers are about 1–3 mm (e.g. Li et al., 2003; Koulali et al., 2012; Mears et al., 2015) depending on the atmospheric water vapor content, with Glowacki et al. (2006) finding the errors were 8–10%.

Williams et al. (1998) confirmed that GPS-derived ZTDs had strong agreements with the Treuhaft and Lanyi (1987) statistical model both temporally and spatially. To be used for InSAR atmospheric corrections the ZTDs must be interpolated, and Williams et al. (1998) showed that the quality of the interpolated ZTDs improves with increasing density of GPS stations and improved accuracy of the ZTD estimates. However, only 20 stations were used in their study and the interpolator was subject to the Southern California region they considered. Li et al. (2006b) developed a GPS topography-dependent turbulence model with a linear height scaling function which reduced water vapor effects on SAR interferograms from ~10 mm to ~5 mm. However, the optimum values for the predefined parameters are sensitive to the local environment and are thus difficult to determine, and one value does not always represent the whole area of interest. Onn and Zebker (2006) used a frozen-flow air assumption plus exponential function for modeling GPS zenith wet delays, which improved the interferograms by 43% in terms of phase variations. Reuveni et al. (2015) applied an exponential function but with different scale factors for the dry and wet components of ZTD which corrected, on average, 17% of the interferogram tropospheric noise. It should be noted that none of the abovementioned GPS correction models has considered the issue of quality control when routinely using GPS to reduce atmospheric effects on repeat-pass InSAR observations. This is mainly because: (i) the model performance is highly dependent on the spatial distribution of GPS stations (e.g. Li et al., 2006b), (ii) the model performance ranges from place to place and from time to time, and (iii) there is a lack of performance indicators to inform users when the correction is applicable. For example, Chen et al. (2010) and Fornaro et al. (2015) blindly applied GPS-based tropospheric corrections, but without any assessment of their applicability or quality which may result in increased noise if errors are present in the GPS derived ZTD corrections. This is confirmed by Chang and He (2011) who found their InSAR results were degraded after applying GPS-based tropospheric delays without first considering the correction model's quality. Furthermore, few previous models have accounted for both the stratified and turbulent components of the tropospheric delay, e.g. Houlié et al. (2016) applied GPS-based tropospheric corrections and reduced phase variations by 51%, but used a uniform Kriging interpolator which does not consider the stratified component of the tropospheric delays and therefore may fail if there are large topography variatons.

More and more continuous GPS networks are becoming available in different regions/countries with increasing density (although still variable from place to place). Meanwhile, a series of SAR missions (e.g. Sentinel-1A/1B, ALOS-2, TerraSAR-X/TanDEM-X, COSMO-SkyMED, RADARSAT-2, and Gaofen-3) are (or have been) operational with some datasets being freely available to the public on a global scale (e.g. Sentinel-1A/1B). It is therefore clear that there is an urgent need to integrate InSAR with GPS in a routine way for precise deformation mapping, and which includes the successful separaration of both the stratified and turbulent tropospheric delay components without predefined local parameters. In this paper, we aim to develop a framework to routinely use GPS to reduce tropospheric effects on radar measurements so to obtain better InSAR displacement products, as follows:

(1) The Iterative Tropospheric Decomposition (ITD) interpolation model developed by Yu et al. (2017) is utilized (and further developed for applicability to relative delays for InSAR) to better separate both stratified and turbulent components from the total tropospheric delays without using predefined local parameters, and then as a spatial interpolator to generate total delay maps from both dense and sparse networks and in either flat or topography variation areas;
(2) Cross validation is employed to assess the performance of the ITD model, which can be considered as a model performance indicator to inform users when the ITD correction is applicable. The performance of the InSAR tropospheric corrections is assessed by considering both the phase standard deviation and the agreement with GPS-measured displacements;
(3) Tests are carried out to assess the impact of GPS station spacing on the performance of the ITD based InSAR tropospheric correction, which provides insights into the tradeoff between station spacing and the achievable accuracy.

2. Tropospheric noise modeling for repeat-pass InSAR

Tropospheric artifacts in SAR interferograms are mainly due to spatial-temporal changes in the refractive index of the medium. These changes are mainly caused by variations in atmospheric pressure, temperature and water vapor. Based on the geometrical configuration of repeat-pass SAR interferometry, the interferometric phase can be written as ϕ (Zebker et al., 1997):

$$\Delta\phi = \phi_1 - \phi_2 = \frac{4\pi}{\lambda}(\boldsymbol{r}_1 - \boldsymbol{r}_2) - \frac{4\pi}{\lambda}(\Delta L_1^{LOS} - \Delta L_2^{LOS}) \quad (1)$$

where λ is the wavelength of the radar signal; $\mathbf{r}_1$ and $\mathbf{r}_2$ are the slant range vectors corresponding to the first and second acquisitions, respectively; $\Delta L_1{}^{LOS}$ and $\Delta L_2{}^{LOS}$ are atmospheric propagation delays of radar signals in the line of sight (LOS). The slant tropospheric delays are computed from the integral between the surface elevation z_0 and the top of the troposphere (Berrada Baby et al., 1988):

$$\Delta L^{LOS} = 10^{-6}\int_{z_0}^{\infty} N dz = 10^{-6}\left[\frac{k_1 R_d}{g_m}P(z_0) + \int_{z_0}^{\infty}\left(k_2'\frac{e}{T} + k_3\frac{e}{T^2}\right)dz\right]M_e \quad (2)$$

where $P(z_0)$ is the surface pressure in Pa; N is the refractive index; g_m is the gravitational acceleration averaged over the troposphere in ms^{-2}; e is the water vapor pressure in Pa; T is the temperature in K; M_e is the mapping function that projects ZTDs to slant total delays based on elevation angles. The remaining terms are constants, i.e., $R_d = 287.05$ J kg^{-1} K^{-1}, $k_1 = 0.776$ K Pa^{-1}, $k_2' = 0.233$ K Pa^{-1}, and $k_3 = 3.75 \times 10^3$ K^2 Pa^{-1}.

Profiles of the Earth's atmosphere show varying degrees of stratification at a wide range of vertical scales, which can introduce a long-term bias in estimates of strain accumulating rates (Doin et al., 2009). When considering local scales (such as an interferogram), this stratification may be substantially disturbed by tropospheric turbulence. Reasons for tropospheric turbulence include, but are not limited to: i) local weather conditions with strong water vapor variations, leading to turbulent fluctuations of temperature and humidity (Tarayre and Massonnet, 1996); ii) scintillation, vertical wind shear force or strong convective effects due to thin turbulent layers in cumulus clouds (Anber et al., 2014); iii) variations of local land covers and ecosystems resulting in localized variations of surface temperature and humidity (Mahmood et al., 2014). Tarayre and Massonnet (1996) reported that a 150 mm/h rainfall can create a 1.8 cm phase shift whilst shear turbulence can cause a 4.4 cm shift if the disturbance extends vertically over 2 km. Hence both the stratified and turbulent components can contribute substantially to the ZTD and must be considered in InSAR atmospheric correction models.

The atmospheric delays in repeat-pass InSAR derived surface displacements (σ_L) are, in dimensions of length, given by $(\lambda/4\pi)\sigma_L$, where λ is the wavelength, with such errors caused by the relative tropospheric delay ($\Delta L_1^{LOS} - \Delta L_2^{LOS}$) occurring between two image acquisitions. Hence GPS-based tropospheric corrections should be provided as high spatial resolution maps of LOS relative delays to enable pixel by pixel correction. This is obtained by interpolating pointwise relative ZTDs (differenced per GPS station between image acquisitions i and j) from the continuously operating GPS stations across and around the area of the interferogram, then mapping to LOS. The ITD model developed by Yu et al. (2017) for the interpolation of undifferenced ZTDs may also be used (after modification) for the interpolation of relative ZTDs, including the separation of the stratified and turbulent components, as follows.

The ITD model considers the relative ZTD between image pair i and j at pixel k with coordinate vector $\mathbf{x}$ to be represented as:

$$\Delta L_{ij}^{k} = \mathrm{S}(h_k) + \mathrm{T}(\mathbf{x}_k) + \varepsilon \quad (3)$$

where S represents the stratified component correlated with height h, T represents the turbulent component and ε is the unmodeled residual. The stratified component in Eq. (3) can be fitted with a modified exponential height scaling function (Xu et al., 2011):

$$\mathrm{S}(h_k) = L_0 \exp\{-\beta(h_k - h_{\min})/(h_{\max} - h_{\min})\} \quad (4)$$

where S is the stratified delay component at sea level and β and L_0 are estimated exponential coefficients for the region considered via regression of the relative ZTDs from a set of GPS stations.

The main procedure of ITD is to iteratively estimate the height scaling function (Eq. (4)) and find the optimal parameters (L_0,β). The turbulent part is then horizontally interpolated and removed from the total delay. To start with, ITD supposes no turbulence signal exists so a pair of (L_0,β) can be obtained. The residuals are then tested by the inverse distance weighting (IDW) law (e.g. Janssen et al., 2004; Li et al., 2006b) to identify the turbulence signal, which is removed from the total delay to generate an updated stratified delay. Several iterations of these steps are made until stable coefficients are obtained. The final output is a set of exponential coefficients (L_0,β) for the given region, plus the turbulent delay and residual per GPS station. Then, both the converged turbulent delay components and residuals from all GPS stations are interpolated to pixel k, and added to the stratified delay computed for height h using the estimated coefficients (L_0,β), and the two summed to produce the relative ZTD per pixel.

A consideration for the ITD model was the choice of turbulent component interpolator. Spline or bilinear interpolators are best for gradually varying surfaces but not appropriate when there are large changes within a short horizontal distance because of over smoothing, which make them less suitable for extreme weather conditions (Akima, 1978; Janssen et al., 2004; Ouassou et al., 2015). Janssen et al. (2004) revealed that IDW and ordinary Kriging interpolation models have similar performance, and are better than spline interpolation for discrete GPS networks. However, ordinary Kriging relies on the estimation of a spatial autocorrelation matrix which is a very computationally intensive process and unmanageable for large datasets (Janssen et al., 2004; Ouassou et al., 2015). Li et al. (2006b) also showed the success of IDW to model GPS-based turbulent delays. As a result, the IDW interpolator is used in the ITD model.

In order to apply the ITD model to InSAR atmospheric correction, we apply a constant value to the relative ZTDs input, and then map to LOS using a tropospheric mapping function. The constant applied will not affect the final result after shifting back but provides the advantage of avoiding negative values in the exponential function regression. We must also consider which GPS reference stations' ZTD values are needed in order to interpolate to the pixel of interest. This depends on the network density, i.e. for a dense network a smaller distance is used, however, for a sparse network, a larger distance is used to ensure that more stations are employed. While Yu et al. (2017) used a maximum distance of 100 km, this was for a dense California network, but as we consider both a dense and sparse network in this paper, we use a maximum distance of 200 km from the particular pixel. This ensures sufficient stations in the sparse network are included, but not those that would be completely uncorrelated with the user station.

3. Cross validation of interpolated tropospheric delays

To assess the capability of the ITD model for handling relative ZTDs, a cross validation was applied to the ITD interpolated values from two different GPS networks. The first is a subset of the Plate Boundary Observatory network, selecting the Southern California region (32° 40′ to 34° 40′ N, 116 to 119° W) of around 250 × 250 km, i.e. about the size of a Sentinel-1A image. It comprises 294 continuous GPS (CGPS) stations, thus providing a very dense network with a station spacing of typically 10–20 km, exhibits large topography variations (from sea level to 3500 m) and experiences a variety of weather/climate conditions in winter and summer seasons. The second is a relatively sparse network, comprising all (up to 141) stations from the UK British Isles continuous GNSS Facility (BIGF: www.bigf.ac.uk) network, which has a typical station spacing of 50–100 km and is more representative of the CGPS station spacing in many countries than the dense Southern California spacing. It also exhibits only limited topography variations (from sea level to 1300 m, but with median elevation only 120 m), and is a cooler atmosphere that can hold less water vapor than Southern California.

All available GPS data from the stations of the Southern California and UK networks for all of 2015 were processed separately per day using the PANDA software package (Liu and Ge, 2003) in Precise Point Positioning mode, with JPL 'repro2' satellite orbits and 30 s clocks, obtained through the International GNSS Service (IGS), held fixed. A least squares adjustment was used for the daily parameter estimation, which comprised constant (float) ambiguities, one set of station coordinates, receiver clocks (estimated as a white noise parameter), and tropospheric zenith wet delay (ZWD) estimated per 5 min epoch as a random walk parameter with a process noise of 5.0e–8 $km/s^{1/2}$, as well

as east-west and north-south tropospheric gradients. We used the ionospherically-free carrier phase and pseudorange observables, employed the Global Mapping Function (GMF: Böhm et al., 2006), applied models for satellite and receiver antenna phase center models (from the IGS), Earth tide (McCarthy, 1996), ocean tide loading (FES2004, from http://holt.oso.chalmers.se/loading), phase wind up (Beyerle, 2009), relativistic effects and pseudorange Differential Calibration Delays (Kouba and Heroux, 2001).

All PANDA-derived GPS ZTDs at 14:00 local time per day were firstly differenced by every 12 days (i.e. between days 1 and 13, 2 and 14, 3 and 15, etc.) in year 2015. We chose 12 day ZTD time differencing to match the repeat cycles of Sentinel-1A, and 14:00 local time provided daily estimates sampled when tropospheric activity and water vapor content was typically greatest. These relative ZTDs were then used for cross validation (Williams et al., 1998) which involved removing a sampled point from the data set and using all the other station relative ZTD values (within the defined correlation distance limit of 200 km) to determine the interpolated relative ZTD at that point using the ITD model. This procedure was repeated for all sampled points, i.e. all stations from both the Southern California and UK networks for the whole of 2015.

The difference between the interpolated and actual 12-day relative ZTDs was computed per station for each of the two GPS networks at 14:00 local time on each day, and the RMS and mean absolute difference (hereafter referred as Mean Absolute Error (MAE)) computed per network per day. These cross validation results, for the whole of 2015, are shown in Fig. 1. For the Southern California network, 94% of the RMS values and 99% of the MAE values are below 1 cm, indicating a high performance of the ITD model interpolator. The overall mean RMS and MAE are 6.9 mm and 5.2 mm, respectively. The ITD model performed better in colder seasons (i.e. between days 0 to 160 and 280 to 365), which we attribute to medium-to-long wavelength and elevation-dependent signals dominating and which were effectively modeled. However, the RMS/MAE are fairly high between day 160 and 280, i.e. the summer months of June to September when the water vapor content is high, implying that the short-wavelength water vapor effects were significant and variable during this period and cannot be fully mitigated by the ITD model. It can be seen from Fig. 1 that the performance was slightly lower in the UK compared with Southern California because of its greater station spacing (50–100 km compared with 10–20 km). 60% of the RMS values and 95% of the MAE values are below 1 cm and the overall RMS and MAE values are 9.7 mm and 6.9 mm, respectively. These results are however still promising for InSAR atmospheric correction which typically aims for (sub-) cm-level precision (Li et al., 2006a; Li et al., 2006b; Onn and Zebker, 2006). The seasonal signal was not as obvious as for Southern California due to different climate features, for example, the precipitation in the UK is nearly stationary during the year whilst the water vapor content in summer is typically 2–3 times higher than winter in Southern California. The greater station spacing in the UK makes it harder to model short-to-medium-wavelength tropospheric delays, resulting in higher RMS and MAE values.

The ITD model interpolation performance was also assessed using a correlation analysis between the interpolated relative ZTDs and the original values, which are plotted for all stations for 14:00 local time for all of 2015 in Fig. 2. The overall cross validation RMS differences of the 12-day relative ZTDs is only 6.2 mm for the Southern California network and 9.7 mm for the UK network. The slopes are close to one with an intercept of zero for both networks, implying that there is no substantial deviation after interpolation. Fig. 2c and d show the RMS distribution of ITD model interpolated relative ZTD of each station for both networks. One clear pattern is that more precise interpolated relative ZTDs are generated in areas with a denser station distribution. In terms of terrain effects on the RMS difference, stations in mountainous areas show approximately comparable precision with those in flat areas, indicating that the performance of the ITD model is nearly independent of height for these networks. The different performance between Southern California and the UK provides an indication of the impact of station distribution as well as the different climate conditions on the ITD model's performance.

4. InSAR atmospheric correction

In order to evaluate the suitability of the ITD model for InSAR atmospheric correction, five Sentinel-1A interferograms (three over Southern California, USA, and two over Southern England, UK, see Table 1) were selected. We chose these interferograms to sample different climate and weather conditions in summer and winter seasons, cool and warm atmospheres, as well as different station densities and topography variations. The interferogram processing was undertaken

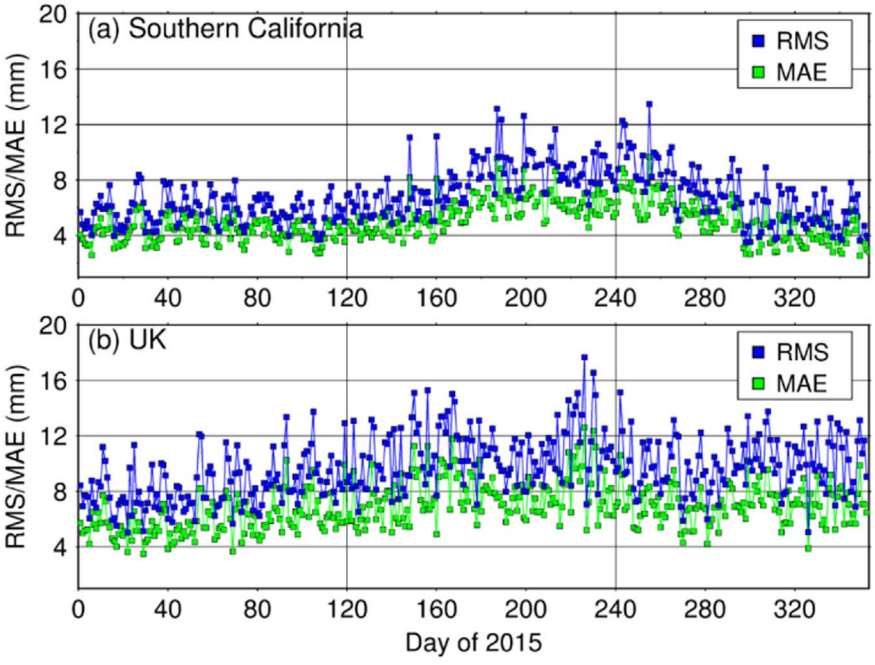

Fig. 1. Daily RMS (blue) and MAE (green) of the 12-day ITD model interpolated relative ZTDs in 2015 compared with the actual relative ZTDs. (a) Southern California GPS network. (b) UK GPS network. The horizontal axis represents the first day that the ZTD is differenced, i.e. day 1 represents the relative ZTD between days 1 and 13. (For interpretation of the references to color in this figure legend, the reader is referred to the web version of this article.)

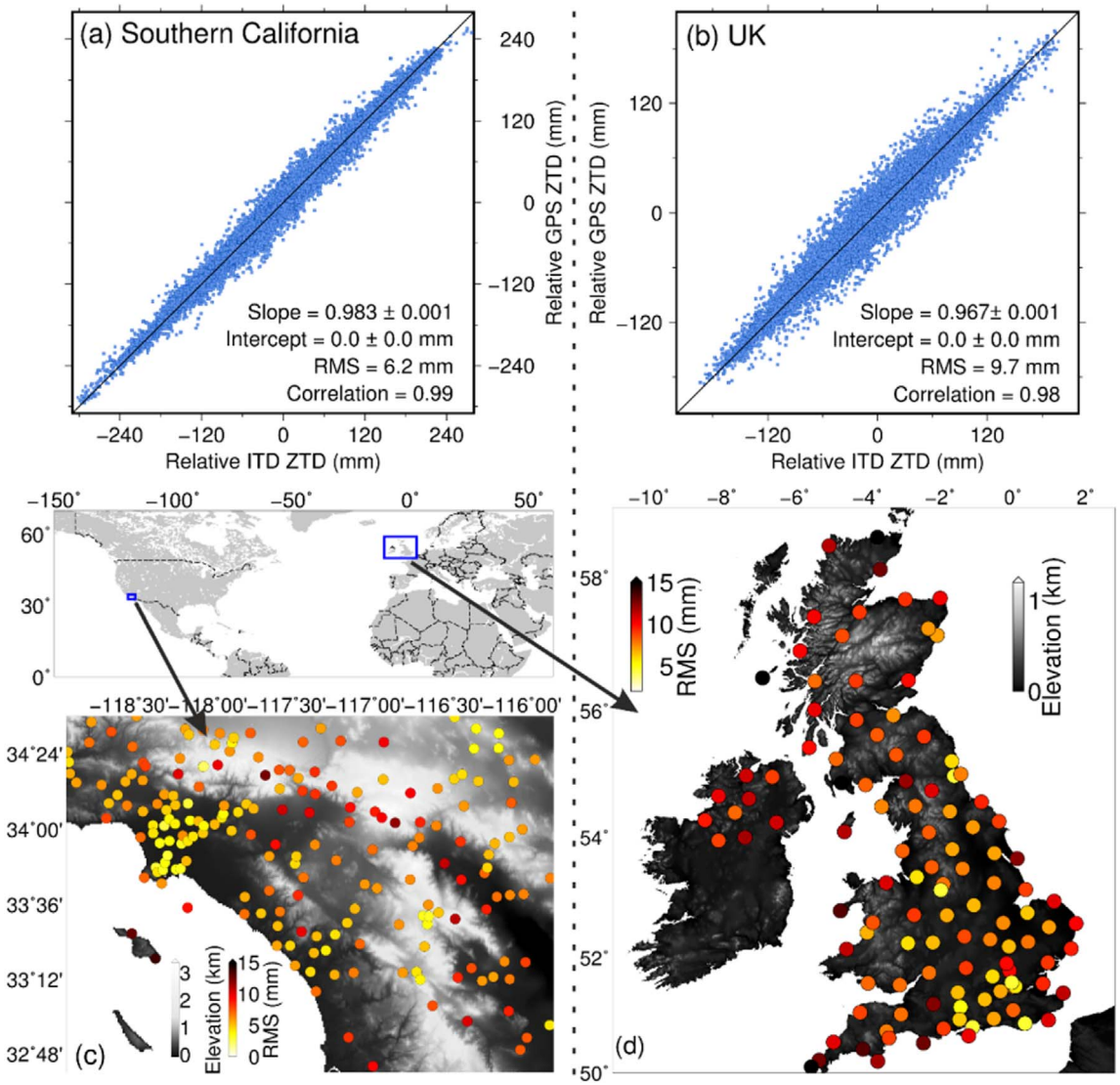

Fig. 2. Cross validation of 12-day ITD model interpolated relative ZTDs for all of 2015 for Southern California (10–20 km station spacing) and UK (50–100 km station spacing) GPS networks, compared with the actual relative ZTDs. The linear model in (a) and (b) is GPS-ZTD = Slope × (Interpolated ZTD) + Intercept. (c) and (d) show the average RMS errors for all of 2015 per station. Note the different map scales.

using the GAMMA software (http://www.gamma-rs.ch), with precise orbit data from the European Space Agency (ESA) used to reduce baseline errors and assist image co-registration and flat earth phase removal. The topographic phase contribution was removed using a 1-arcsec (~30 m) DEM from the Shuttle Radar Topography Mission (Farr et al., 2007). The interferometric pairs were processed by multi-looking operation with 10 pixels in the azimuth direction and two pixels in the range direction, and then unwrapped by the branch-cut method with the coherence threshold set to 0.5 (Goldstein et al., 1988). The ITD model was utilized to generate relative ZTD maps for all the five interferograms; the relative ZTDs were projected to the LOS direction of the InSAR observations with the GMF mapping function, and then applied as the interferogram atmospheric corrections per pixel (one point every ~30 m). It should be noted that the unwrapped phase was converted to range changes in the LOS where a positive range change indicates the Earth's surface is moving away from the satellite (or an increase in the delay of radar propagation due to the atmosphere). Since the ITD model is able to separate stratified delays from the turbulent component, stratified delay maps were also generated to investigate the impact of tropospheric turbulence on InSAR observations.

To assess the performance of the ITD model, two metrics were used. The LOS range change standard deviation (hereafter called StdDev)

Table 1
Sentinel-1A interferograms (denoted as Ifg) used in this study.

Ifg	Orbit	Date 1	Date 2	Δt (days)	Location	Geographical extent
Ifg1	Ascending	26/05/2015	29/10/2015	156	Southern California	32–35 N, 116–119 W
Ifg2	Ascending	13/07/2015	25/07/2015	12	Southern California	32–35 N, 116–119 W
Ifg3	Descending	16/12/2015	21/03/2016	96	Southern California	33–36 N, 116–119 W
Ifg4	Ascending	30/01/2015	07/03/2015	36	Southern England	51–54 N, 1–3 W
Ifg5	Ascending	01/01/2016	25/01/2016	24	Southern England	50–53 N, 2 W–2 E

across the entire interferogram was computed to assess the precision, which assumed there was negligible ground movement between the two image acquisitions (12–156 days). As a large StdDev could also result from actual ground movements such as interseismic slip or ground water extraction (e.g. Argus et al., 2005; Sneed et al., 2014), to account for this and assess the accuracy, the InSAR displacements at each GPS station location were compared with independent 3D GPS-derived displacements provided by the Nevada Geodetic Laboratory at the University of Nevada, Reno (Blewitt et al., 2016). Both InSAR and GPS-derived displacements were converted to LOS, differenced for all GPS stations in the interferogram, and the RMS displacement difference computed. Note that all stations (within the defined 200 km decorrelation range limit) from the GPS networks were used to generate the correction maps for interferograms, but only the stations located inside the interferogram were used when computing the RMS differences. We hereafter categorise stations with displacement improvements greater than twice the RMS difference (2RMS) per corrected interferogram as substantial improvements.

4.1. Atmospheric correction using the dense GPS network in Southern California

Fig. 3 shows the three Southern California interferograms with and without the GPS-based ITD model atmospheric correction. Ifg1, which spans a time interval of 156 days from 25 May 2015 (dry season) to 29 October 2015 (rainy season), shows in its raw form (Fig. 3a, with no atmospheric correction) a range increase (up to 6.4 cm, i.e. the Earth surface moving towards the radar sensor) around San Bernardino National Forest, together with a range decrease (up to − 4.9 cm, i.e. the Earth surface moving away the radar sensor) around Palm Desert. After correcting with the stratified delays only (Fig. 3b) and then the ITD model total (stratified and turbulent) delays (Fig. 3c), both clustering features still exist, but their magnitudes decrease, with the StdDev reducing from 1.69 cm to 1.45 cm and 1.05 cm, respectively. At the GPS stations, the RMS displacement difference reduced from 1.66 cm to 1.47 cm after applying the stratified correction only, and further to 0.92 cm after applying the total delay correction, indicating that the ITD model reduced the large variances around San Bernardino National Forest and Palm Desert mainly by modeling the troposphere turbulence. 72% of stations exhibited substantial (> 2RMS) improvements after correcting with total delays compared to 57% with the correction using the stratified part only. Moreover, accounting for the tropospheric turbulence reduced the percentage of stations with deteriorated performance from 11% to 3%. Note that Sneed et al. (2014) reported that the Coachella Valley (close to Palm Desert) is subducting due to reduced groundwater-levels, as observed both by InSAR and GPS methods, which may be associated with the remaining LOS displacement signal in the corrected map of Fig. 3c.

Ifg2 was obtained from images 12 days (one orbital period) apart in July, i.e. the summer, when the atmosphere can hold most water vapor. A prominent long-wavelength signal was observed across the whole raw interferogram (Fig. 3d), with an inhomogeneous pattern with clear gradients towards the center of the area, and troughs around the Palm Desert and the Anza-Borrego Desert. The RMS displacement difference was 3.85 cm and the phase StdDev was 3.72 cm, indicating substantial tropospheric noise contamination. After applying the ITD model total delay (Fig. 3f), the RMS difference reduced to 0.84 cm and the StdDev to 1.75 cm. Overall, 63% of stations exhibited RMS improvements greater than 2RMS after correcting with the total delays compared to 23% with the stratified part only. Moreover, accounting for the troposphere turbulence reduced the percentage of stations at which deterioration arose (after applying the tropospheric corrections compared with applying none) from 14% with stratified delays only, to 2%. Unlike for Ifg1, the major improvement came from the turbulent delay correction (RMS difference reduction from 3.85 cm to 0.84 cm with the total delays, but only reduced to 2.67 cm with the stratified delays) and the GPS stations which exhibited > 2RMS improvements only arose after correcting with the total delays (and not with the stratified part only), indicating that substantial atmospheric turbulence occurred during this short 12 day time-differencing interval. These strong turbulent signals are most likely caused by conditions when the 23 July 2015 radar image was acquired, since a rainfall event was reported during 18–21 July 2015 (www.wunderground.com/).

Ifg3 was obtained from two images in rainy seasons with a time interval of 96 days. As can be seen from Fig. 3g, the phase measurements exhibit a clear long-wavelength pattern along the southwest to northeast direction, which is probably due to atmospheric errors considering the relatively short time span. The RMS displacement difference reduced by 68% from 2.32 cm to 0.75 cm after correcting with the total delays and by 54% to 1.07 cm with only the stratified delays, respectively. The long-wavelength pattern seen in Fig. 3g has been mostly eliminated on correcting with only the stratified delays, but a further 14% improvement was achieved when correcting using the total delays. 74% of the GPS stations experienced greater than 2RMS displacement improvements after correcting with total delays compared with 59% on only correcting with the stratified component delays. Moreover, accounting for the troposphere turbulence reduced the percentage of stations at which deteriorations occurred from 7% to 2%. Similarly, the LOS range change StdDev was reduced from 2.18 cm for the raw interferogram, to 1.08 cm on correcting with the stratified delays only, to 0.85 cm when using the total delays, i.e. respective 50% and 61% improvements (Table 2).

To further consider the improvement obtained for the InSAR-derived displacements at the GPS stations after applying the atmospheric corrections in all three interferograms, the differences between InSAR and GPS displacements in the LOS direction at 127 GPS stations for all three interferograms Ifg1-3 are shown in Fig. 4, with no tropospheric corrections (i.e. raw), correcting with the stratified delays only, and correcting with the total delays. The overall RMS difference between InSAR and GPS displacements improved from 3.79 cm with no atmospheric corrections, to 1.86 cm on correcting with stratified delays only, to 0.87 cm on correcting with the total delays. It can be seen from Fig. 4 that differences of around 7 cm still arise in some instances if only the stratified delay is applied, further illustrating the need to consider and successfully correct both the stratified and turbulent components.

4.2. Atmospheric correction using the sparse GPS network in southern England

To assess whether the substantial improvements obtained on correcting the Southern California interferograms (with the dense 10–20 km GPS station spacing) are also obtained for a sparser GPS network, we applied the ITD atmospheric corrections to two Southern England interferograms, with a station spacing of 50–80 km. The maximum spacing of 80 km for this part of the UK network is slightly less than the 100 km maximum spacing that arises in some parts of the UK network. For both interferograms (Ifg4 and Ifg5 in Fig. 5), the LOS range change StdDev was reduced to below 1 cm after correcting with the total delays (from a StdDev of 2.56 cm and 4.76 cm for the respective two raw interferograms, representing improvements of 65–79%), whilst applying the stratified delay corrections only led to StdDev values of 1.3–1.5 cm. Similarly, the RMS LOS displacement differences were improved from 2.72 cm and 2.42 cm (raw) to 1.79 cm and 1.45 cm respectively on applying the stratified delays only, to 0.80 cm and 0.97 cm when applying the total delays, representing improvements of about 60–70% (Table 2). The short time intervals of 24 and 36 days between the image acquisitions used for the two interferograms means that actual ground movements should be negligible, and the atmosphere-corrected maps confirm this hypothesis more strongly than the raw interferograms, as can be seen from Fig. 5. It can also be seen from Fig. 5 that the proportion of GPS stations with more than 2RMS displacement difference improvements increases from 32%

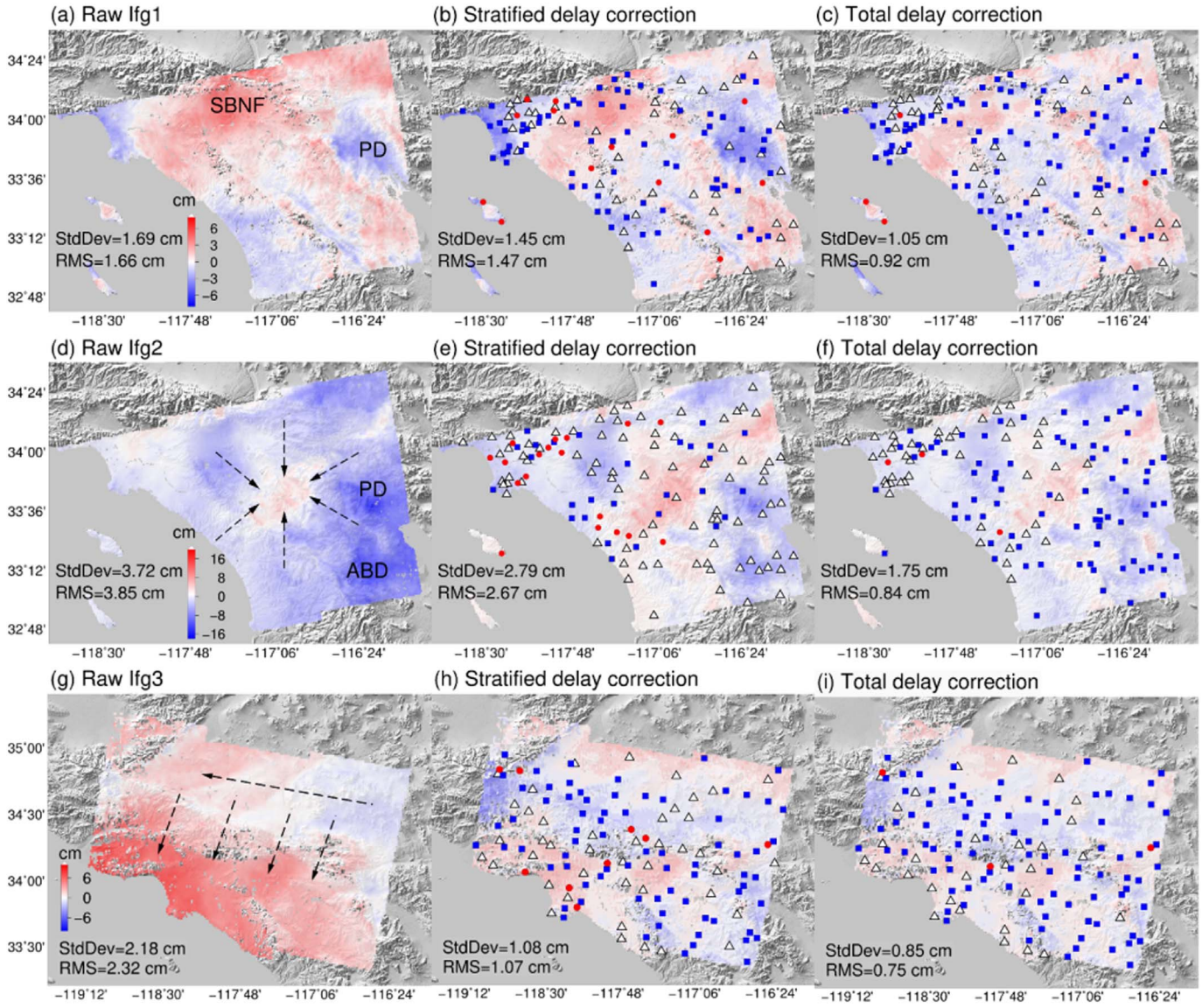

Fig. 3. Southern California Sentinel-1A interferograms. (a, d, g) Raw; (b, e, h) corrected only by the stratified delays from the ITD model; (c, f, i) corrected by the total delays from the ITD model. SBNF: San Bernardino National Forest; PD: Palm Desert; ABD: Anza-Borrego Desert. The LOS range change StdDev and the RMS difference between GPS and InSAR displacements are listed per interferogram per tropospheric correction approach. White triangles, blue squares and red solid circles in (b, e, h) and (c, f, i) represent GPS stations with displacement improvement < 2RMS, > 2RMS, and deterioration, after correction, respectively. Note the different color bars.

and 50% on correcting with the stratified delays only, to 73% and 69% on correcting with the total delays. Finally, the raw and corrected displacement differences are collated for both interferograms in Fig. 5g, with the raw overall RMS displacement difference reducing from 2.36 cm to 1.69 cm and 0.81 cm on applying the stratified delays and total delays, respectively. These statistics illustrate the capability of the ITD model to be applied to relatively sparse GPS networks, which are commonly distributed globally. The impact of GPS station density is further considered in Section 5.

4.3. Features of tropospheric turbulence

Substantial improvements to InSAR displacement maps have been obtained after applying atmospheric corrections with both dense and

Table 2
Performance of ITD model stratified and total delay atmospheric corrections on the interferograms. Unit: cm. Numbers in parentheses indicate the percentage improvement, (Raw – Corrected)/Raw.

Interferograms	Phase StdDev			Displacement RMS		
	Raw Ifg	Stratified correction	Total delay correction	Raw Ifg	Stratified correction	Total delay correction
Ifg1	1.69	1.45 (14%)	1.05 (38%)	1.66	1.47 (11%)	0.92 (45%)
Ifg2	3.72	2.79 (25%)	1.75 (53%)	3.85	2.67 (31%)	0.84 (78%)
Ifg3	2.18	1.08 (50%)	0.85 (61%)	2.32	1.07 (54%)	0.75 (68%)
Ifg4	2.56	1.50 (41%)	0.90 (65%)	2.72	1.79 (34%)	0.80 (71%)
Ifg5	4.76	1.30 (73%)	0.98 (79%)	2.42	1.45 (40%)	0.97 (59%)
Mean	2.98	1.62 (46%)	1.11 (63%)	2.59	1.69 (35%)	0.86 (67%)

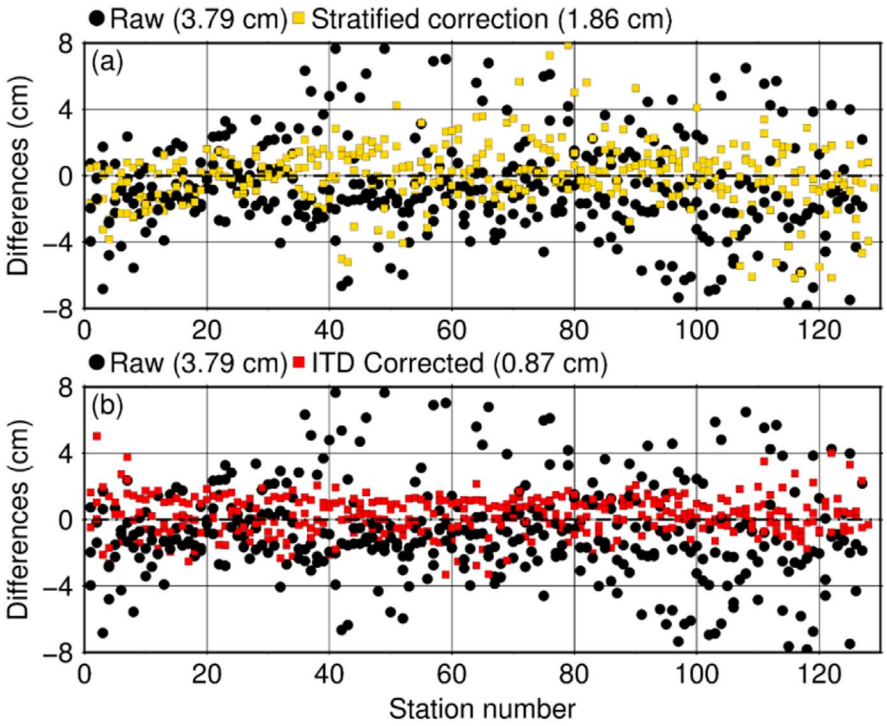

Fig. 4. Differences between InSAR and GPS LOS displacements after ITD model atmospheric correction with (a) stratified delays and (b) total delays, respectively, collated for all three Southern California interferograms. Numbers in parentheses indicate the overall RMS differences. The horizontal axes represent the 127 stations.

sparse GPS networks. In theory, a denser network can reveal topography-related tropospheric signals better and capture the turbulence features in greater detail, especially in mountainous areas. Most likely due to a lack of high resolution ZTD maps, turbulent signals have previously commonly been considered as a random process with a Gaussian distribution and either reduced by averaging or stacking (e.g. Fruneau and Sarti, 2000; Ferretti et al., 2011) or simply ignored (e.g. Elliott et al., 2008; Doin et al., 2009). However, our experiments show that turbulent delays can exhibit non-random patterns in space and account for a large proportion (e.g. up to 72% for Ifg2) of the total delays. This is especially true given the fact that the atmospheric effects on repeat-pass InSAR observations are differenced (between two image acquisitions) and part of the stratified components can be canceled out, leaving the turbulent effects as dominant. In Sections 4.1 and 4.2, we have demonstrated the presence of turbulent signals and the improvements arising to interferograms if atmospheric corrections using the total delays, not just the stratified delays, are applied. Here we further discuss the turbulent signal features and their impact on InSAR atmospheric corrections.

Fig. 6 shows the stratified and turbulent components of relative ZTD for all GPS stations in the three Southern California interferograms. For Ifg1, the average percentages of the total delay made up by the turbulent and stratified components are nearly identical (49% against 51%, Fig. 6a) and there is no clear pattern for the turbulent part. However, a strong turbulent pattern can be observed for Ifg2 with the turbulent component contributing on average 72% of the total delay (Fig. 6b). A clear turbulent pattern can also be seen in Fig. 6c where some of the stations suffer from substantial atmospheric delay increases while others exhibit substantial decreases. We attribute this mainly to the crowded tropospheric delays in the shore area where the turbulence behavior is completely different from that in the inland area. On correcting with the stratified delays only, such as would be obtained via correlation analysis between interferometric phases and elevations (as used by for example Elliott et al., 2008 and Doin et al., 2009), only limited RMS LOS displacement reductions can be obtained (Fig. 3). The turbulent part also helped to reduce the tropospheric delay clustering on certain topographies such as the forest and desert in Ifg1. It is therefore clear that correcting with only the stratified delay component is far from optimal for mitigating InSAR atmospheric effects.

Fig. 7 shows the spatial distribution of the tropospheric turbulence signals on the Southern California interferograms, and the key features can be summarized as:

1). The turbulent components can have a comparable magnitude to the elevation-dependent component (i.e. stratified delays, see Figs. 3 and 6). This is mainly because the differencing in InSAR weakens the stratification but, to some extent, amplifies the turbulence, especially when the weather conditions on the two days of image acquisition are considerably different and hence the errors tend towards a random distribution.

2). Patterns of the turbulent delays arise, with decreasing delays around the Palm Desert in Fig. 7a and Fig. 7b and the Anza-Borrego Desert in Fig. 7b, and increasing delays around San Bernardino National Forest in Fig. 7a and the shore areas, as shown in Fig. 7c. The turbulent delays are sometimes clustered into different groups all with their own peak values. The distribution of tropospheric turbulence is inhomogeneous, making it challenging to interpret actual deformation signals in InSAR measurements if they are not appropriately mitigated.

3). More variable turbulence can be seen in the summer than in other seasons (see the magnitude scales in Fig. 7, where Ifg2 is in the summer) due to the atmosphere being able to hold more water vapor. This is consistent with the findings in previous works (e.g. Li et al., 2006a; Xu et al., 2011).

5. Assessment of the impact of station spacing

As shown in Section 4, all the five interferograms were improved after applying the ITD model atmospheric corrections. The Southern California interferograms covered a region of varying topography but with a dense GPS network, whilst the Southern England region had a sparser GPS network but with flatter terrain. In order to assess the impact of station distribution on the ITD model performance, a station spacing test was carried out for the Southern California network. It

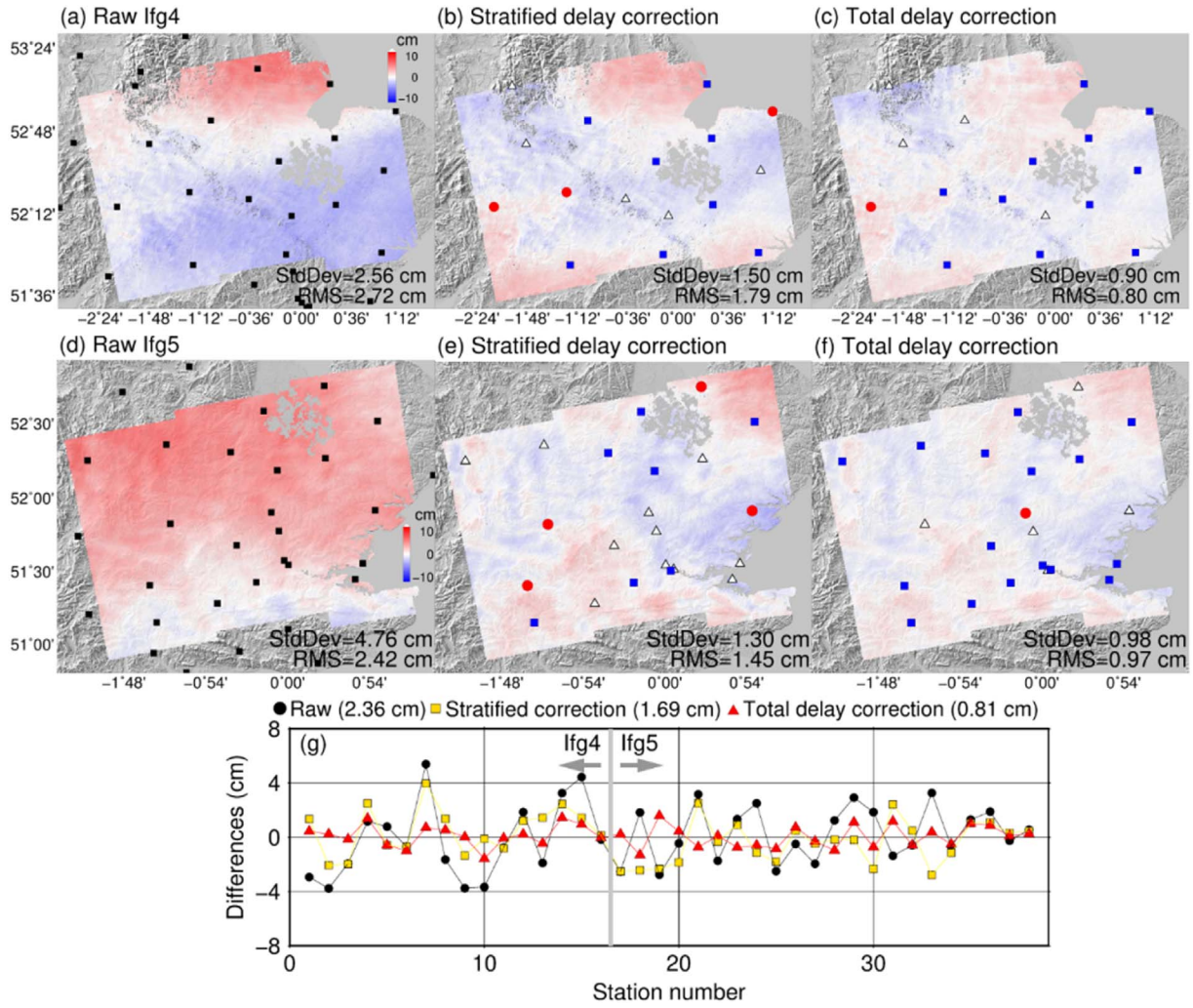

Fig. 5. Southern England Sentinel-1A interferograms. (a, d) Raw; (b, e) corrected only by the stratified delays from the ITD model; (c, f) corrected by the total delays from the ITD model. The LOS range change StdDev and the RMS difference between GPS and InSAR displacements are listed per interferogram per tropospheric correction approach. White triangles, blue squares and red solid circles in (b, e) and (c, f) represent GPS stations with displacement improvement < 2RMS, > 2RMS, and deterioration, after correction, respectively. Note the different color bars. (g) Collated differences for both interferograms.

comprised deleting stations from the (dense) network covered by the interferogram, to form sub-networks with different station spacing. The procedure was as follows: (i) we divided the whole coverage area into uniform grids for a chosen station spacing distance (1 km, 2 km, 3 km, etc.); (ii) for each grid, we selected only one station inside it (the closest one from the grid center) and all the selected stations were then used to form a new sub-network; (iii) by repeating the previous two steps, we generated a series of sub-networks with different station spacings ranging from 1 km to 70 km. The station spacing here means the size of each grid and, to some extent, represents the average distance between stations. This procedure ensured resampling of stations as uniformly as possible, leaving the spacing distance as the main variable between the sub-networks.

Fig. 8 shows some results of the spacing test with three sub-networks used to generate ITD model total delays and applied to the three Southern California interferograms, plotted for station spacing

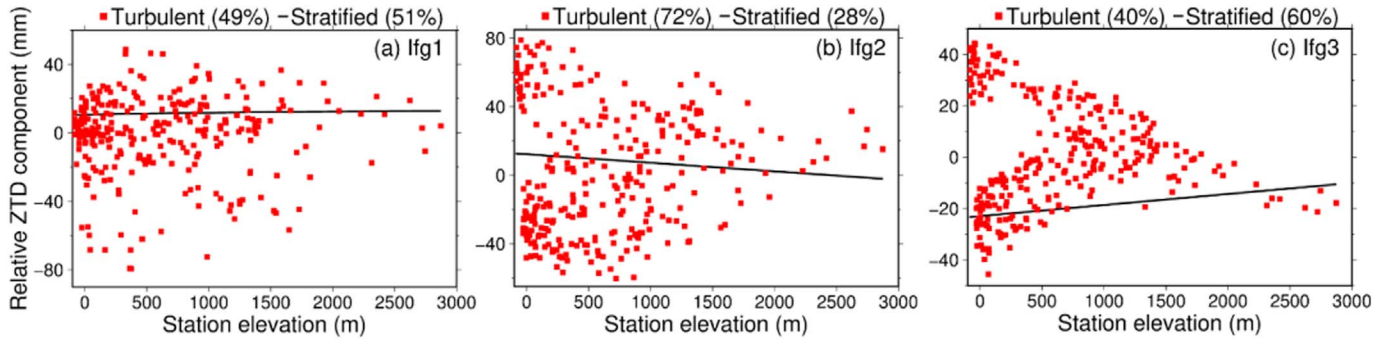

Fig. 6. Turbulent and stratified components of the relative ZTDs, as separated by the ITD model with all the available GPS stations in the three Southern California interferograms (Ifg1-3). The listed percentages denote the average proportion of the total delay contributed by the stratified and turbulent components. Note the different ZTD ranges.

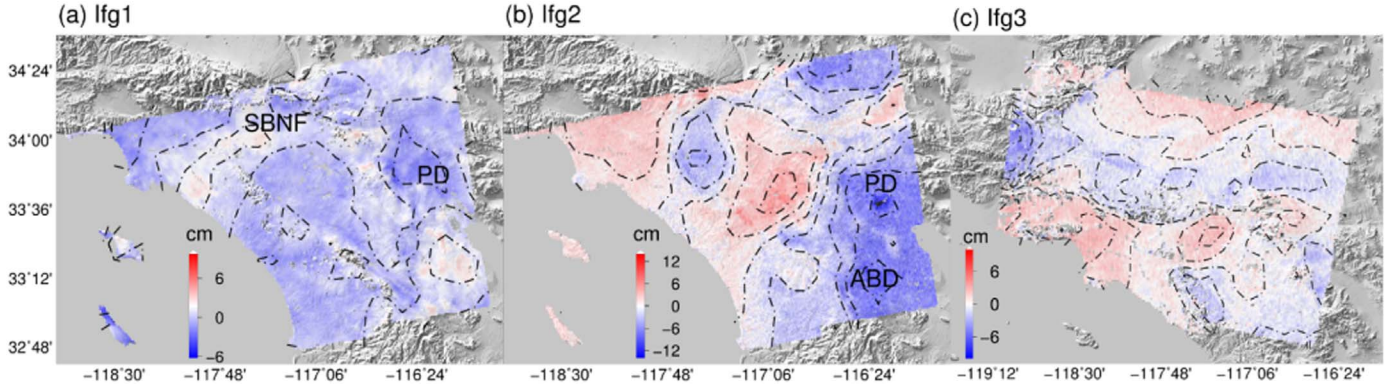

Fig. 7. Turbulent relative zenith delays estimated using the ITD model for the three Southern California interferograms, Ifg1-3. The black dotted lines represent turbulent delay contours of 1 cm; SBNF = San Bernardino National Forest, PD = Palm Desert, ABD = Anza-Borrego Desert. Note the different color bars.

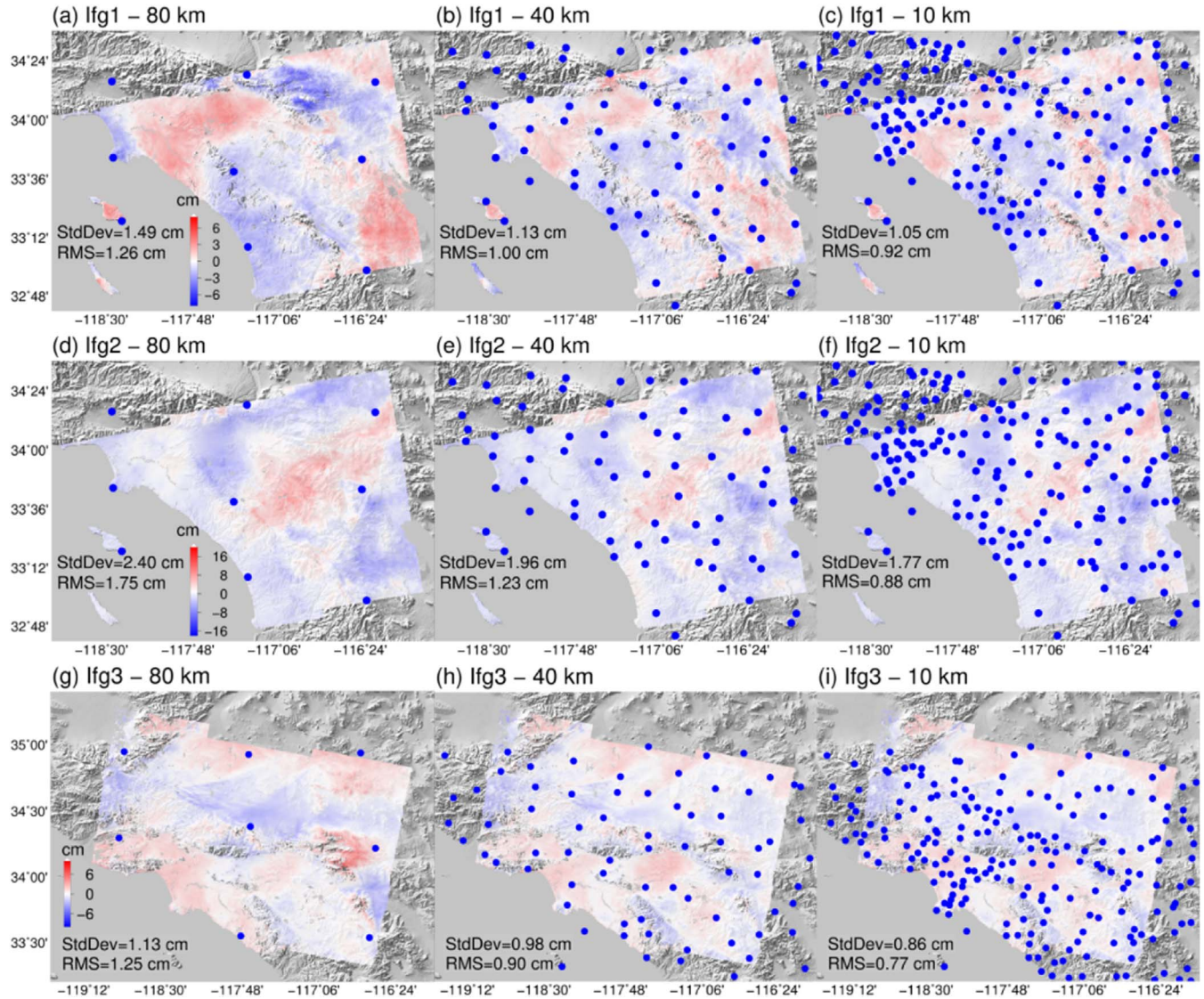

Fig. 8. GPS station spacing tests on the Southern California interferograms. Three sub-networks were considered with spacing distances of 80 km, 40 km and 10 km, with the blue dots representing the GPS stations used to compute the ITD model total delay corrections applied in each interferogram. The corrected interferograms and the corresponding phase StdDev and RMS displacement difference statistics are also indicated. Note the different color bars per interferogram. (For interpretation of the references to color in this figure legend, the reader is referred to the web version of this article.)

Table 3
Summary of station spacing tests for the Southern California interferograms. Unit: cm. The number in parentheses indicates the improvement, (Raw – Corrected)/Raw.

Interferograms	Phase StdDev	Displacement RMS
Ifg1 - Raw	1.69	1.66
Ifg1 – 80 km	1.49 (12%)	1.26 (24%)
Ifg1 – 40 km	1.13 (33%)	1.00 (40%)
Ifg1 – 10 km	1.05 (38%)	0.92 (45%)
Ifg2 - Raw	3.72	3.85
Ifg2 – 80 km	2.40 (35%)	1.75 (55%)
Ifg2 – 40 km	1.96 (47%)	1.23 (68%)
Ifg2 – 10 km	1.77 (52%)	0.88 (77%)
Ifg3 - Raw	2.18	2.32
Ifg3 – 80 km	1.13 (48%)	1.25 (46%)
Ifg3 – 40 km	0.98 (55%)	0.90 (61%)
Ifg3 – 10 km	0.86 (61%)	0.77 (67%)

distances of 80 km, 40 km and 10 km. The performance improves dramatically as the spacing decreases from 80 km to 40 km (LOS range change StdDev improving from 1.49, 2.40 and 1.13 cm, to 1.13, 1.96 and 0.96 cm, respectively for interferograms Ifg1-3; RMS LOS displacement differences improving from 1.26, 1.75 and 1.25 cm, to 1.00, 1.23 and 0.90 cm, respectively), but little further improvement was attained when further decreasing the spacing from 40 km to 10 km, as can be seen in Fig. 8 and Table 3. This indicates that some medium-to-long wavelength signals are not handled well by the sparsely distributed pointwise ZTDs, although even this 80 km spacing provides improvements over the raw interferogram, e.g. for Ifg2 the StdDev and RMS difference improved from 3.85 and 3.72 cm to 2.40 and 1.75 cm, respectively. By adding stations uniformly until a 40 km spacing was attained enabled the overall tropospheric noise to be modeled as much as possible by the network. A denser network with 10 km distance had a similar performance, revealing that short-wavelength turbulent signals are hard to model even with a very dense GPS network.

More detailed statistics of the spacing test are shown in Fig. 9. Fig. 9a represents the relative ZTD cross validation RMS differences (using the three interferograms) for each sub-network with spacing distance ranging from 2 km to 80 km at a 1 km interval. Fig. 9b shows the noise reduction level of each sub-network and the improvement percentage, calculated as the LOS range change StdDev and RMS LOS displacement difference reduction divided by the maximum reduction. Limited improvement was obtained on decreasing the spacing from 15 km due to (i) the additional stations were located in areas where the tropospheric delays had already been fully modeled (it should be noted that the station distribution in our original network is not uniform) so that contributed no further improvement; (ii) the principal component of tropospheric delay signals has already been modeled and the closer distance between stations contributed only limited improvement on modeling short wavelength signals. When the spacing is below 15 km, the performance remains similar to when the principal component of tropospheric delay signals is modeled. However, as the distance increased from 15 km the performance degraded, with the increased spacing distance resulting in fewer stations being available, which made the correction maps less reliable. This can be seen from the more variable performance between 50 and 80 km, i.e. although some sub-networks have similar spacing, their performance can be totally different.

The spacing test serves as an intuitive way to understand the impact of the station distribution on the ITD model performance. A good distribution should be able to model the principal components of tropospheric noise, i.e. as the spacing distance decreases, the ZTD cross validation RMS should converge before the number of stations converges and therefore adding more stations would introduce little improvement. In the case that the stations are distributed rather non-uniformly, the conclusions still hold except that the largest noise reduction will converge to a local optimum, leaving some medium-to-long wavelength noise signal still being uncorrected, especially those areas where few or no stations are available.

6. Conclusions and outlook

In this paper, we have demonstrated a framework to routinely use GPS to reduce tropospheric effects on radar measurements. The Yu et al. (2017) Iterative Tropospheric Decomposition (ITD) model was employed to separate the turbulent and stratified delays from the total delays and then further developed in order to reduce their coupling effects on SAR interferograms. Cross validation and station spacing tests were carried out to serve as indicators of correction performance to inform users whether the correction is applicable and provide insights

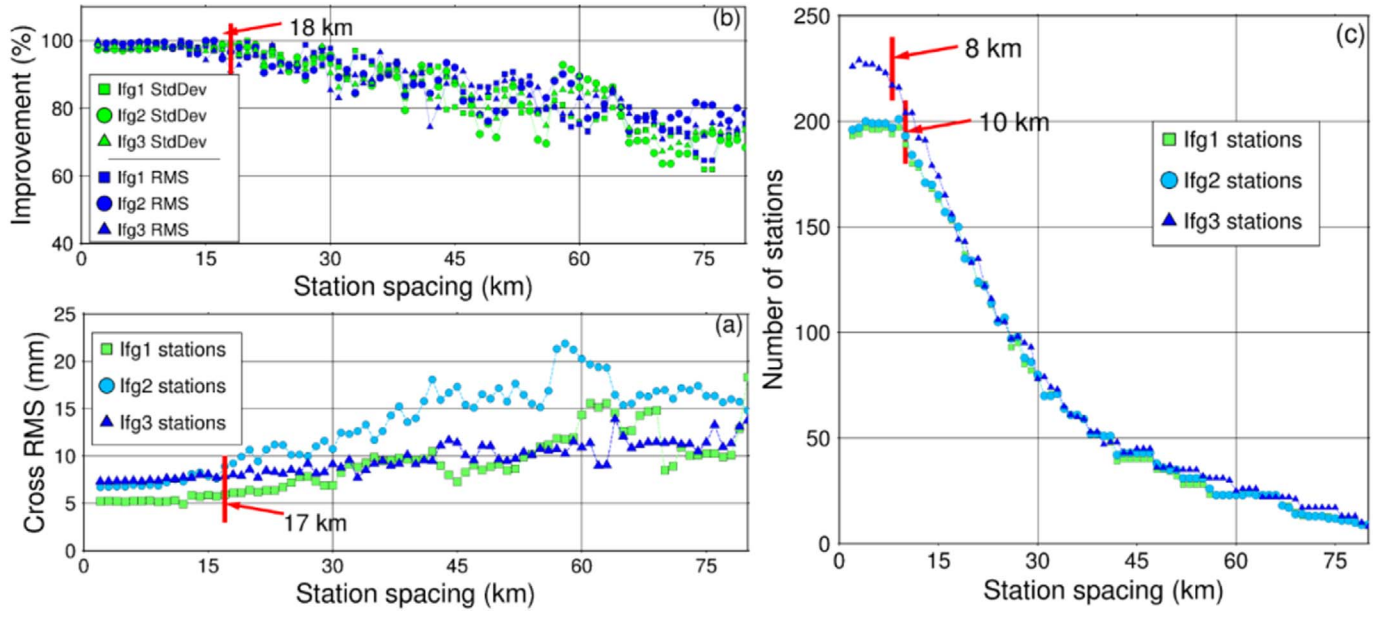

Fig. 9. Multiple station spacing tests for the three Southern California interferograms, ranging from 2 km to 80 km. (a) Relative ZTD cross validation for each sub-network on every interferogram. (b) Noise reduction using each sub-network stations on every interferogram, for phase (StdDev) and RMS difference between InSAR and GPS LOS displacements. (c) number of stations for each sub-network with different station spacings.

into the trade-off between station spacing and the achievable accuracy.

After applying our GPS-based tropospheric correction model (using the total delays, i.e. including both the stratified and turbulent components), the RMS differences between InSAR and GPS displacements in the LOS for five Sentinel-1A interferograms in Southern California (10–20 km station spacing) and Southern England (50–80 km station spacing) reduced from 1.66, 3.85, 2.32, 2.72 and 2.42 cm, to 0.92, 0.84, 0.75, 0.80 and 0.97 cm, respectively. These represented improvements of 45–79% for Southern California, and 59–71% for Southern England, and the phase standard deviation improvements for the two test areas were 38–61% and 65–79%, respectively. These are greater improvements than the maximum 50% improvements obtained in previous studies, and incorporate both high topography variations (Calfornia) and flatter terrain (Southern England). The importance of correcting for turbulent delays has been emphasized since the time differencing of InSAR can cancel out part of the stratified component and amplify the turbulence effects. The turbulent components can have a comparable magnitude to the stratified component and exhibit larger variations in the summer than in other seasons due to the atmosphere being able to hold more water vapor. By accounting for both the stratification and turbulence of the troposphere, ~1 cm precision of the corrected interferograms is achievable. This improves the feasibility of using InSAR observations to investigate low-amplitude, long-wavelength deformation fields such as those due to inter-seismic strain accumulation and/or post-seismic motion, and to investigate the underground human activities in modern cities which plays an important role in ground subsidence monitoring (e.g. Crosetto et al., 2002; Walters et al., 2013; Chen et al., 2016). Futhermore, this method does not result in any removal of real deformation signals or require manual interaction, which can arise when using filtering tropospheric mitigation approaches, and unlike using MERIS and MODIS, is applicable in all weathers.

The proposed framework enables the GPS-based tropospheric correction model to be used routinely in a systematic, automatic way, in order to mitigate the inherent GPS-based model limitations and to avoid its application in such scenarios whereby poor correction performance would result. ZTD cross validation provides an assessment of the overall interpolation performance which should be considered as one essential step to assess the feasibility of the ITD model correction. A lower RMS in the cross validation indicates higher ITD model performance, and vice versa (Fig. 9). Spacing tests served as an intuitive way to understand how the station distribution affects the correction performance, which is especially important when using pointwise GPS ZTDs which may be sparsely or non-uniformly distributed. A network with a greater station spacing is likely to provide higher RMS values and hence poorer correction performance against a denser network. Based on these two indicators, one could decide whether the correction is applicable as well as assessing the expected accuracy of the network considered.

The ITD model offers an excellent opportunity to integrate multiple water vapor products with GPS, such as those from the European Centre for Medium-Range Weather Forecasts (ECMWF) numeral weather model and Moderate Resolution Imaging Spectroradiometer (MODIS). ECMWF-ZTD and/or MODIS near-IR PWV may be input to the ITD model in the same way as pointwise GPS ZTDs but with different weighting strategies. Their combination should enable the spatial resolution attainable when using only sparse GPS networks to be improved, and to improve the temporal resolution attainable when using only ECMWF or MODIS. It is suggested that their combination could lead to a generic InSAR atmospheric correction model with all-weather and continuous global availability.

Acknowledgements

The GPS data sets and orbit/clock products used in this paper were gratefully obtained from the PBO (pbo.unavco.org), NERC BIGF (www.bigf.ac.uk) and the IGS. Sentinel-1A images were provided freely by ESA's Sentinels Scientific data Hub. This work was supported by a Chinese Scholarship Council studentship (ref. 201506270155) awarded to Chen Yu. Part of this work was also supported by the UK NERC through the Centre for the Observation and Modelling of Earthquakes, Volcanoes and Tectonics (COMET, ref.: come30001) and the LICS and CEDRRIC projects (ref. NE/K010794/1 and NE/N012151/1, respectively), and the ESA-MOST DRAGON-4 project (ref. 32244). Thanks also to Paola Crippa for her helpful suggestions and comments. The figures were generated using the Generic Mapping Tools software (Wessel et al., 2013).

References

Akima, H., 1978. A method of bivariate interpolation and smooth surface fitting for irregularly distributed data points. ACM Trans. Math. Softw. 4 (2), 148–159.
Anber, U., Wang, S., Sobel, A., 2014. Response of atmospheric convection to vertical wind shear: cloud-system-resolving simulations with parameterized large-scale circulation. Part I: specified radiative cooling. J. Atmos. Sci. 71 (8), 2976–2993.
Argus, D.F., Heflin, M.B., Peltzer, G., Crampé, F., Webb, F.H., 2005. Interseismic strain accumulation and anthropogenic motion in metropolitan Los Angeles. J. Geophys. Res. Solid Earth. 110, B04401.
Bastin, S., Champollion, C., Bock, O., Drobinski, P., Masson, F., 2007. Diurnal cycle of water vapor as documented by a dense GPS network in a coastal area during ESCOMPTE IOP2. J. Appl. Meteorol. 46 (2), 167–182.
Béjar-Pizarro, M., Socquet, A., Armijo, R., Carrizo, D., Genrich, J., Simons, M., 2013. Andean structural control on interseismic coupling in the North Chile subduction zone. Nat. Geosci. 6, 462–467.
Bekaert, D.P.S., Hooper, A., Wright, T.J., 2015a. A spatially variable power law tropospheric correction technique for InSAR data. J. Geophys. Res. Solid Earth 120 (2), 1345–1356.
Bekaert, D.P.S., Walters, R.J., Wright, T.J., Hooper, A.J., Parker, D.J., 2015b. Statistical comparison of InSAR tropospheric correction techniques. Remote Sens. Environ. 170, 40–47.
Berrada Baby, H., Gole, P., Lavergnat, J., 1988. A model for the tropospheric excess path length of radio waves from surface meteorological measurements. Radio Sci. 23 (6), 1023–1038.
Beyerle, G., 2009. Carrier phase wind-up in GPS reflectometry. GPS Solutions 13 (3), 191–198.
Blewitt, G., Kreemer, C., Hammond, W.C., Gazeaux, J., 2016. MIDAS robust trend estimator for accurate GPS station velocities without step detection. J. Geophys. Res. Solid Earth 121, 2054–2068.
Böhm, J., Niell, A., Tregoning, P., Schuh, H., 2006. Global Mapping Function (GMF): a new empirical mapping function based on numerical weather model data. Geophys. Res. Lett. 33 (7).
Chang, L., He, X., 2011. InSAR atmospheric distortions mitigation: GPS observations and NCEP FNL data. J. Atmos. Sol. Terr. Phys. 73 (4), 464–471.
Chen, Q., Liu, G., Ding, X., Hu, J.-C., Yuan, L., Zhong, P., Omura, M., 2010. Tight integration of GPS observations and persistent scatter InSAR for detecting vertical ground motion in Hong Kong. Int. J. Appl. Earth Obs. Geoinf. 12 (6), 477–486.
Chen, F., Lin, H., Zhou, W., Hong, T., Wang, G., 2013. Surface deformation detected by ALOS PALSAR small baseline SAR interferometry over permafrost environment of Beiluhe section, Tibet Plateau, China. Remote Sens. Environ. 138, 10–18.
Chen, M., Tomás, R., Li, Z., Motagh, M., Li, T., Hu, L., Gong, H., Li, X., Yu, J., Gong, X., 2016. Imaging land subsidence induced by groundwater extraction in Beijing (China) using satellite radar interferometry. Remote Sens. 8 (6), 468.
Crosetto, M., Tscherning, C.C., Crippa, B., Castillo, M., 2002. Subsidence monitoring using SAR interferometry: reduction of the atmospheric effects using stochastic filtering. Geophys. Res. Lett. 29 (9).
Delacourt, C., Briole, P., Achache, J.A., 1998. Tropospheric corrections of SAR interferograms with strong topography. Application to Etna. Geophys. Res. Lett. 25 (15), 2849–2852.
Ding, X.L., Li, Z.W., Zhu, J.J., Feng, G.C., Long, J.P., 2008. Atmospheric effects on InSAR measurements and their mitigation. Sensors 8 (9), 5426–5448.
Doin, M.P., Lasserre, C., Peltzer, G., Cavalié, O., Doubre, C., 2009. Corrections of stratified tropospheric delays in SAR interferometry: validation with global atmospheric models. J. Appl. Geophys. 69 (1), 35–50.
Elliott, J.R., Biggs, J., Parsons, B., Wright, T.J., 2008. InSAR slip rate determination on the Altyn Tagh Fault, northern Tibet, in the presence of topographically correlated atmospheric delays. Geophys. Res. Lett. 35 (12).
Farr, T.G., Rosen, P.A., Caro, E., Crippen, R., Duren, R., Hensley, S., Kobrick, M., Paller, M., Rodriguez, E., Roth, L., Seal, D., Shaffer, S., Shimada, J., Umland, J., Werner, M., Oskin, M., Burbank, D., Alsdorf, D., 2007. The shuttle radar topography mission. Rev. Geophys. 45 (2).
Ferretti, A., Prati, C., Rocca, F., 2001. Permanent scatterers in SAR interferometry. IEEE Trans. Geosci. Remote Sens. 39 (1), 8–20.
Ferretti, A., Fumagalli, A., Novali, F., Prati, C., Rocca, F., Rucci, A., 2011. A new algorithm for processing interferometric data-stacks: SqueeSAR. IEEE Trans. Geosci. Remote Sens. 49 (9), 3460–3470.
Fornaro, G., D'Agostino, N., Giuliani, R., Noviello, C., Reale, D., Verde, S., 2015. Assimilation of GPS-derived atmospheric propagation delay in DInSAR data processing. IEEE J. Sel. Top. Appl. 8 (2) (874-799).
Fruneau, B., Sarti, F., 2000. Detection of ground subsidence in the city of Paris using radar interferometry: isolation of deformation from atmospheric artifacts using correlation.

Geophys. Res. Lett. 27 (24), 3981–3984.
Glowacki, T.J., Penna, N.T., Bourke, W.P., 2006. Validation of GPS-based estimates of integrated water vapour for the Australian region and identification of diurnal variability. Aust. Meteorol. Mag. 55, 131–148.
Goldstein, R.M., Zebker, H.A., Werner, C.L., 1988. Satellite radar interferometry: two-dimensional phase unwrapping. Radio Sci. 23 (4), 713–720.
Hooper, A., Zebker, H., Segall, P., Kampes, B., 2004. A new method for measuring deformation on volcanoes and other natural terrains using InSAR persistent scatterers. Geophys. Res. Lett. 31 (23).
Hooper, A., Bekaert, D., Spaans, K., Arıkan, M., 2012. Recent advances in SAR interferometry time series analysis for measuring crustal deformation. Tectonophysics 514, 1–13.
Houlié, N., Funning, G.J., Bürgmann, R., 2016. Use of a GPS-derived troposphere model to improve InSAR deformation estimates in the San Gabriel Valley, California. IEEE Trans. Geosci. Remote Sens. 54 (9), 5365–5374.
Huang, L., Wen, X., 2014. Temporal variations of atmospheric water vapor δD and $\delta^{18}O$ above an arid artificial oasis cropland in the Heihe River Basin. J. Geophys. Res. Atmos. 119, 11,456–11,476.
Janssen, V., Ge, L., Rizos, C., 2004. Tropospheric corrections to SAR interferometry from GPS observations. GPS Solutions 8 (3), 140–151.
Jolivet, R., Grandin, R., Lasserre, C., Doin, M.P., Peltzer, G., 2011. Systematic InSAR tropospheric phase delay corrections from global meteorological reanalysis data. Geophys. Res. Lett. 38 (L17311).
Jolivet, R., Agram, P.S., Lin, N.Y., Simons, M., Doin, M.-P., Peltzer, G., Li, Z., 2014. Improving InSAR geodesy using Global Atmospheric Models. J. Geophys. Res. Solid Earth 119, 2324–2341.
Kouba, J., Heroux, P., 2001. Precise point positioning using IGS orbit and clock products. GPS Solutions 5 (2), 12–18.
Koulali, A., Ouazar, D., Bock, O., Fadil, A., 2012. Study of seasonal-scale atmospheric water cycle with ground-based GPS receivers, radiosondes and NWP models over Morocco. Atmos. Res. 104, 273–291.
Li, Z., Muller, J.P., Cross, P., 2003. Comparison of precipitable water vapor derived from radiosonde, GPS, and Moderate-Resolution Imaging Spectroradiometer measurements. J. Geophys. Res. Atmos. 108 (D20).
Li, Z., Muller, J.P., Cross, P., Fielding, E.J., 2005. Interferometric synthetic aperture radar (InSAR) atmospheric correction: GPS, Moderate Resolution Imaging Spectroradiometer (MODIS), and InSAR integration. J. Geophys. Res. Solid Earth 110 (B3).
Li, Z., Muller, J.P., Cross, P., Albert, P., Fischer, J., Bennartz, R., 2006a. Assessment of the potential of MERIS near-infrared water vapour products to correct ASAR interferometric measurements. Int. J. Remote Sens. 27 (2), 349–365.
Li, Z., Fielding, E.J., Cross, P., Muller, J.P., 2006b. Interferometric synthetic aperture radar atmospheric correction: GPS topography-dependent turbulence model. J. Geophys. Res. Solid Earth 111 (B2).
Li, Z., Fielding, E.J., Cross, P., Preusker, R., 2009. Advanced InSAR atmospheric correction: MERIS/MODIS combination and stacked water vapour models. Int. J. Remote Sens. 30, 3343–3363.
Li, Z.W., Xu, W.B., Feng, G.C., Hu, J., Wang, C.C., Ding, X.L., Zhu, J.J., 2012. Correcting atmospheric effects on InSAR with MERIS water vapour data and elevation-dependent interpolation model. Geophys. J. Int. 189 (2), 898–910.
Liu, J., Ge, M., 2003. PANDA software and its preliminary result of positioning and orbit determination. Wuhan Univ. J. Nat. Sci. 8 (2B), 603–609.
Lu, Z., Dzurisin, D., Biggs, J., Wicks, C., McNutt, S., 2010. Ground surface deformation patterns, magma supply, and magma storage at Okmok volcano, Alaska, from InSAR analysis: 1. Intereruption deformation, 1997–2008. J. Geophys. Res. Solid Earth 115 (B5).
Mahmood, R., et al., 2014. Land cover changes and their biogeophysical effects on climate. Int. J. Climatol. 34 (4), 929–953.
Massonnet, D., Feigl, K.L., 1998. Radar interferometry and its application to changes in the Earth's surface. Rev. Geophys. 36 (4), 441–500.
Massonnet, D., Feigl, K., Rossi, M., Adragna, F., 1994. Radar interferometric mapping of deformation in the year after the Landers earthquake. Nature 369 (6477), 227–230.
McCarthy, D.D., 1996. IERS Conventions (1996). IERS Technical Note 21. In: US Naval Observatory.
Mears, C.A., Wang, J., Smith, D., Wentz, F.J., 2015. Intercomparison of total precipitable water measurements made by satellite-borne microwave radiometers and ground-based GPS instruments. J. Geophys. Res.-Atmos. 120 (6), 2492–2504.
Onn, F., Zebker, H.A., 2006. Correction for interferometric synthetic aperture radar atmospheric phase artifacts using time series of zenith wet delay observations from a GPS network. J. Geophys. Res. Solid Earth 111 (B9).
Ouassou, M., Jensen, A.B.O., Gjevestad, J.G.O., Kristiansen, O., 2015. Next generation network real-time kinematic interpolation segment to improve the user accuracy. Int. J. Navig. Observation 2015 (3), 1–15.
Rao, V.B., Cavalcanti, I.F., Hada, K., 1996. Annual variation of rainfall over Brazil and water vapor characteristics over South America. J. Geophys. Res. Atmos. 101 (D21), 26539–26551.
Reuveni, Y., Bock, Y., Tong, X., Moore, A.W., 2015. Calibrating interferometric synthetic aperture radar (InSAR) images with regional GPS network atmosphere models. Geophys. J. Int. 202 (3), 2106–2119.
Shirzaei, M., Bürgmann, R., 2012. Topography correlated atmospheric delay correction in radar interferometry using wavelet transforms. Geophys. Res. Lett. 39 (L01305).
Short, N., LeBlanc, A.M., Sladen, W., Oldenborger, G., Mathon-Dufour, V., Brisco, B., 2014. RADARSAT-2 D-InSAR for ground displacement in permafrost terrain, validation from Iqaluit Airport, Baffin Island, Canada. Remote Sens. Environ. 141, 40–51.
Simons, M., Rosen, P.A., 2007. Interferometric synthetic aperture radar geodesy. In: Schubert, G. (Ed.), Treatise on Geophysics, pp. 391–446.
Sneed, M., Brandt, J.T., Solt, M., 2014. Land subsidence, groundwater levels, and geology in the Coachella Valley, California. 1993–2010 (No. 2014-5075). In: US Geological Survey.
Tarayre, H., Massonnet, D., 1996. Atmospheric propagation heterogeneities revealed by ERS-1 interferometry. Geophys. Res. Lett. 23 (9), 989–992.
Treuhaft, R.N., Lanyi, G.E., 1987. The effect of the dynamic wet troposphere on radio interferometric measurements. Radio Sci. 22 (2), 251–265.
Walters, R.J., Elliott, J.R., Li, Z., Parsons, B., 2013. Rapid strain accumulation on the Ashkabad fault (Turkmenistan) from atmosphere-corrected InSAR. J. Geophys. Res. Solid Earth 118 (7), 3674–3690.
Wessel, P., Smith, W.H.F., Scharroo, R., Luis, J., Wobbe, F., 2013. Generic mapping tools: improved version released. Eos. Trans. AGU 94 (45) (409-210).
Williams, S., Bock, Y., Fang, P., 1998. Integrated satellite interferometry: tropospheric noise, GPS estimates and implications for interferometric synthetic aperture radar products. J. Geophys. Res. 103 (B11), 27051–27067.
Xu, W.B., Li, Z.W., Ding, X.L., Zhu, J.J., 2011. Interpolating atmospheric water vapor delay by incorporating terrain elevation information. J. Geod. 85 (9), 555–564.
Yu, C., Penna, N.T., Li, Z., 2017. Generation of real-time mode high-resolution water vapor fields from GPS observations. J. Geophys. Res. Atmos. 22, 2008–2025. http://dx.doi.org/10.1002/2016JD025753.
Zebker, H.A., Rosen, P.A., Hensley, S., 1997. Atmospheric effects in interferometric synthetic aperture radar surface deformation and topographic maps. J. Geophys. Res. Solid Earth 102 (B4), 7547–7563.